# A Comparative L-dwarf Sample Exploring the Interplay between Atmospheric Assumptions and Data Properties

Eileen C. Gonzales[1,2,7] , Ben Burningham[3] , Jacqueline K. Faherty[2] , Nikole K. Lewis[1] , Channon Visscher[4,5] , and Mark Marley[6]
[1] Department of Astronomy and Carl Sagan Institute, Cornell University, 122 Sciences Drive, Ithaca, NY 14853, USA; ecg224@cornell.edu
[2] Department of Astrophysics, American Museum of Natural History, New York, NY 10024, USA
[3] Centre for Astrophysics Research, School of Physics, Astronomy and Mathematics, University of Hertfordshire, Hatfield AL10 9AB, UK
[4] Chemistry & Planetary Sciences, Dordt University, Sioux Center, IA, USA
[5] Center for Extrasolar Planetary Systems, Space Science Institute, Boulder, CO, USA
[6] Department of Planetary Sciences and Lunar and Planetary Laboratory, University of Arizona, Tucson, AZ, USA

## Abstract

Comparisons of atmospheric retrievals can reveal powerful insights on the strengths and limitations of our data and modeling tools. In this paper, we examine a sample of five L dwarfs of similar effective temperature ($T_{eff}$) or spectral type to compare their pressure–temperature (P-T) profiles. Additionally, we explore the impact of an object's metallicity and the signal-to-noise ratio (S/N) of the observations on the parameters we can retrieve. We present the first atmospheric retrievals: 2MASS J15261405+2043414, 2MASS J05395200−0059019, 2MASS J15394189−0520428, and GD 165B increasing the small but growing number of L dwarfs retrieved. When compared to the atmospheric retrievals of SDSS J141624.08+134826.7, a low-metallicity d/sdL7 primary in a wide L+T binary, we find that similar $T_{eff}$ sources have similar P-T profiles with metallicity differences impacting the relative offset between their P-T profiles in the photosphere. We also find that for near-infrared spectra, when the S/N is ≳80 we are in a regime where model uncertainties dominate over data measurement uncertainties. As such, S/N does not play a role in the retrieval's ability to distinguish between a cloud-free and cloudless model, but may impact the confidence of the retrieved parameters. Lastly, we also discuss how to break cloud model degeneracies and the impact of extraneous gases in a retrieval model.

*Unified Astronomy Thesaurus concepts:* Brown dwarfs (185); Exoplanets (498); Atmospheric composition (2120); Fundamental parameters of stars (555); L dwarfs (894); Stellar atmospheres (1584); Metallicity (1031)

## 1. Introduction

Brown dwarfs form a crucial link between stars and planets, with masses ranging from ∼ 13 to 75 $M_{Jup}$ and temperatures of ∼250–3000 K (Saumon et al. 1996; Chabrier & Baraffe 1997). With masses below the hydrogen burning limit, their cores never reach the temperature and pressure required for nuclear fusion and instead are sustained by electron degeneracy pressure (Hayashi & Nakano 1963; Kumar 1963). As such, as brown dwarfs age they continuously cool morphing through the spectral sequence of M, L, T, and Y defined by their optical and/or near-infrared (NIR) spectra (Burgasser et al. 2002; Kirkpatrick 2005; Cushing et al. 2011). This lack of sustained stable hydrogen burning in the cores of brown dwarfs leads to a degeneracy between their effective temperature ($T_{eff}$), mass, and age making these parameters difficult to disentangle.

One way to break the degeneracy is by obtaining the kinematics of an object along with its spectrum. Young brown dwarfs can display kinematics placing them in nearby young moving groups (e.g., Faherty et al. 2016; Kellogg et al. 2016; Gagné et al. 2017) or spectral features indicative of youth such as weak alkali lines and enhanced metal oxides (Kirkpatrick et al. 2006; Cruz et al. 2009; Allers et al. 2010). Subdwarfs

display unusually blue NIR colors, metallicities lower than that of the Sun, kinematics placing them in the galactic halo, and spectral features such as weak or absent metal oxides and enhanced metal hydrides (Gizis 1997; Burgasser et al. 2003, 2008; Dahn et al. 2008; Burgasser et al. 2009; Cushing et al. 2009). This has enabled the separation of brown dwarfs into roughly three main age subpopulations–field, young (low-gravity), and subdwarfs (low-metallicity), corresponding to ages of roughly 0.5–10 Gyr (e.g., Filippazzo et al. 2015), <500 Myr (e.g., Bell et al. 2015), and >5 Gyr (e.g., Gonzales et al. 2018), respectively.

With the age groupings determined, many works have examined observational correlations between the bolometric luminosity ($L_{bol}$), $T_{eff}$, spectral type, and colors of these subpopulations. When comparing the NIR color and spectral type, low-gravity sources appear redder than field sources, while subdwarfs appear bluer. Observational studies have led to the creation of polynomial relations for $L_{bol}$, $T_{eff}$, and the magnitude versus spectral type for field, low-gravity sources, and subdwarfs (e.g., Filippazzo et al. 2015; Faherty et al. 2016; Dupuy & Liu 2017; Zhang et al. 2017), as well as the development of gravity sensitive indices (Allers & Liu 2013).

As another way to probe the mass–$T_{eff}$–age degeneracy, comparisons of the spectral energy distributions (SEDs) and the resultant semi-empirical fundamental parameters have been made across objects of similar $L_{bol}$ and $T_{eff}$ (e.g., Filippazzo et al. 2015; Gonzales et al. 2018, 2019). Comparisons highlight the differences in the overall SED shape, as well as the impact clouds, metallicity, and surface gravity play in shaping those

---

differences in NIR spectral bands. For example, Gonzales et al. (2018) highlight the impact clouds have on the overall SED shape for objects of the same $T_{\rm eff}$ but differing ages. They show that cloudy young objects redistribute the flux out to longer wavelengths while low-metallicity objects do not, due to a lack of clouds in their atmospheres.

To more deeply compare the atmospheres of brown dwarfs, we need to move to using a theoretical approach. In this work we use atmospheric retrievals, an in-depth data-driven spectral modeling approach to explore the physical and chemical processes occurring in an object's atmosphere. These processes impact an object's chemical composition, cloud properties, formation, and evolution. By using atmospheric retrievals, we can compare the similarities and differences between the thermal structure of brown dwarfs of similar $T_{\rm eff}$ or spectral type. At present, retrievals of brown dwarfs are still a relatively new approach in the field. There is a growing number of L, T, and Y dwarfs examined (e.g., Line et al. 2014, 2015, 2017; Burningham et al. 2017, 2021; Zalesky et al. 2019; Gonzales et al. 2020, 2021; Kitzmann et al. 2020; Piette & Madhusudhan 2020; Howe et al. 2022; Lueber et al. 2022); however, none of these studies to date have completed a comparison between the retrieved properties with a sample of objects anchored by their observational and fundamental parameter similarities such as what we present in this work.

Using the *Brewster* retrieval framework (Burningham et al. 2017) we pose the question "How do the pressure–temperature (P-T) profiles of objects of similar spectral type or similar $T_{\rm eff}$ compare to one another?" To address this we created a sample anchored by the d/sdL7 dwarf SDSS J141624.08+134826.7 (hereafter J1416+1348A) with one optical spectral type comparison and three $T_{\rm eff}$ comparisons based on the $T_{\rm eff}$ from their SEDs. We chose multiple $T_{\rm eff}$ comparisons for J1416+1348A as its $T_{\rm eff}$ differs by ~200 K between the SED and retrieval methods (Gonzales et al. 2020). In Section 2 we present the literature data on the sample. We present semi-empirical fundamental parameters for the sample generated via the SEDs in Section 3. We discuss the *Brewster* retrieval code framework in Section 4 and present our updates to the Gonzales et al. (2020) retrieval of J1416+1348A in Section 5. Sections 6 and 7 describe the model and results for our comparative sample. Section 8 compares the P-T profiles for the spectral type and $T_{\rm eff}$ samples, discusses the impact of wavelength coverage and metallicity on the shape of the P-T profile, and the impact of the signal-to-noise ratio (S/N) on model selection and the retrieved property constraints.

## 2. Literature Data on Sample

Relevant literature data for the sample is presented in the following subsections and listed in Table 1.

### 2.1. J1416+1348A

J1416+1348A was independently discovered by Burningham et al. (2010), Schmidt et al. (2010), and Bowler et al. (2010). It is spectral typed as d/sdL7 in the optical (Burningham et al. 2010) due to its unusually blue NIR color and spectral features implying a low metallicity and/or high surface gravity (Schmidt et al. 2010). There are currently three optical spectra (Schmidt et al. 2010, SDSS and MagE; Kirkpatrick et al. 2016, Palomar), three NIR spectra (Spex Prism: Bowler et al. 2010; Schmidt et al. 2010, Spex SXD: Schmidt et al. 2010), and

one *L*-band spectrum (Cushing et al. 2010) available for J1416+1348A. Gaia Data Release (DR) 2 provides parallax and proper motion measurements (Gaia Collaboration et al. 2016, 2018; Lindegren et al. 2018) and the Sloan Digital Sky Survey (SDSS) DR7 provides radial velocity measurements (Abazajian et al. 2009; Bowler et al. 2010; Schmidt et al. 2010). Fundamental parameters for J1416+1348A have been determined by fitting its self-consistent grid models to its spectrum (Bowler et al. 2010; Burningham et al. 2010; Cushing et al. 2010; Schmidt et al. 2010) as well as through generating its SED and atmospheric retrievals using the *Brewster* code base (Gonzales et al. 2020). Table 1 lists all the pertinent parameters.

### 2.2. J1526+2043, Optical Spectral Type Comparison

2MASS J15261405+2043414 (hereafter J1526+2043) was discovered by Kirkpatrick et al. (2000) and spectral typed as L7 in the optical (Kirkpatrick et al. 2000) and L5 in the NIR (Schneider et al. 2014). The proper motion of J1526+2043 has been measured by Sheppard & Cushing (2008), Faherty et al. (2009), and Gaia DR2 (Gaia Collaboration et al. 2016, 2018; Lindegren et al. 2018). The parallax has been measured by Faherty et al. (2012) and Gaia DR2. Spectra for J1526+2043 cover wavelengths from ~0.6 to 12 $\mu$m (optical: Kirkpatrick et al. 2000; NIR: Burgasser et al. 2004; mid-infrared (MIR): Cushing et al. 2006). $L_{\rm bol}$, $T_{\rm eff}$, the mass, the radius, and log $g$ for J1526+2043 were initially derived in Filippazzo et al. (2015) via SED generation and are updated in this work. See Table 1 for all relevant parameters of J1526+2043 for this study.

### 2.3. J0539−0059, $T_{eff}$ Comparison

2MASS J05395200−0059019 (hereafter J0539−0059) was discovered by Kirkpatrick et al. (2000) and spectral typed as L5 in the optical (Fan et al. 2000) and L5 in the NIR (Geballe et al. 2002). Spectra (optical: Fan et al. 2000; NIR: Cushing et al. 2005; Schneider et al. 2014; MIR: Cushing et al. 2006; Yamamura et al. 2010) and photometry for J0539−0059 covers ~0.45–12 $\mu$m. Its parallax was measured by Vrba et al. (2004) and Gaia DR2 (Gaia Collaboration et al. 2016, 2018; Lindegren et al. 2018). The radial velocity and $v \sin i$ were measured in Blake et al. (2010), which are listed in Table 1. The fundamental parameters ($L_{\rm bol}$, $T_{\rm eff}$, mass, radius, and log $g$) were determined by Filippazzo et al. (2015) and are updated in this work using the same method.

Bailer-Jones & Mundt (2001) found strong evidence of variability in the *I* band for J0539−0059, with a period of $13.3 \pm 1.2$ hr, which was noted as a possible rotation period. Some evidence of spectral variability due to dust was noted in Bailer-Jones (2008). However, J0539−0059 was found to have marginal evidence for long-timescale variability but no signs of rapid brightness changes in Koen (2013). Furthermore, Buenzli et al. (2014) found no signs of variability in the *J* and *H* bands. Values for J0539−0059 from the literature and this work are listed in Table 1.

### 2.4. J1539−0520, $T_{eff}$ Comparison

2MASS J15394189−0520428 (hereafter J1539−0520) was discovered by Kirkpatrick et al. (2000) and spectral typed as L4 in the optical (Kirkpatrick et al. 2008) and L2 in the NIR (Kendall et al. 2004). Burgasser et al. (2015) noted its

**Table 1**
Selected Literature Data on the Comparative Sample

| Property | J1416+1348A | References | SpT Comp J1526+2043 | References | $T_{\rm eff}$ Comp J0539−0059 | References | J1539−0520 | References | GD 165B | References |
|---|---|---|---|---|---|---|---|---|---|---|
| Optical Spectral Type | d/sdL7 | 1 | L7 | 2 | L5 | 3 | L4 | 4 | L4 | 5 |
| NIR Spectral Type | L6.0pec±2.0 | 6 | L5 | 7 | L5 | 8 | L2 | 9 | L3 | 8 |
| **Astrometry** | | | | | | | | | | |
| R.A. | $14^{\rm h}16^{\rm m}24\overset{s}{.}08$ | 10 | $15^{\rm h}26^{\rm m}14\overset{s}{.}05$ | 10 | $05^{\rm h}39^{\rm m}52\overset{s}{.}00$ | 10 | $15^{\rm h}39^{\rm m}41\overset{s}{.}89$ | 10 | $14^{\rm h}24^{\rm m}39\overset{s}{.}09$ | 10 |
| decl. | $+13°48'26\overset{''}{.}3$ | 10 | $+20°43'41\overset{''}{.}4$ | 10 | $-00°59'01\overset{''}{.}9$ | 10 | $-05°20'42\overset{''}{.}8$ | 10 | $+09°17'10\overset{''}{.}4$ | 10 |
| $\pi$ (mas) | $107.56 \pm 0.30$ | 11 | $50.00 \pm 1.48$ | 11 | $78.53 \pm 0.57$ | 11 | $58.82 \pm 0.42$ | 11 | $29.933 \pm 0.06$ | 11 |
| $\mu_\alpha$ (mas yr$^{-1}$) | $85.69 \pm 0.69$ | 11 | $-220.78 \pm 2.34$ | 11 | $162.45 \pm 0.79$ | 11 | $590.20 \pm 0.75$ | 11 | $-213.35 \pm 0.08$ | 11 |
| $\mu_\delta$ (mas yr$^{-1}$) | $129.07 \pm 0.47$ | 11 | $-359.16 \pm 2.04$ | 11 | $321.15 \pm 0.76$ | 11 | $104.57 \pm 0.73$ | 11 | $-149.65 \pm 0.07$ | 11 |
| $v \sin i$ | ... | ... | ... | .... | $32.30 \pm 0.75$ | 12 | $40.09 \pm 0.76$ | 12 | $18 \pm 2$ | 13 |
| $V_r$ (km s$^{-1}$) | $-42.2 \pm 1.24$ | 14 | ... | ... | $13.91 \pm 0.15$ | 12 | $27.33 \pm 0.24$ | 12 | $-29 \pm 2$ | 15 |
| **Parameters from SED** | | | | | | | | | | |
| $L_{\rm bol}$ | $-4.18 \pm 0.011$ | 16 | $-4.339 \pm 0.022$ | 17 | $-4.18 \pm 0.016$ | 17 | $-3.959 \pm 0.016$ | 17 | $-3.99 \pm 0.04$ | 17 |
| $T_{\rm eff}$ (K) | $1694 \pm 74$ | 16 | $1491 \pm 78$ | 17 | $1633 \pm 68$ | 17 | $1837 \pm 66$ | 17 | $1804 \pm 75$ | 17 |
| Radius ($R_{\rm Jup}$) | $0.92 \pm 0.08$ | 16 | $0.99 \pm 0.10$ | 17 | $0.99 \pm 0.08$ | 17 | $1.01 \pm 0.07$ | 17 | $1.01 \pm 0.07$ | 17 |
| Mass ($M_{\rm Jup}$) | $60 \pm 18$ | 16 | $56 \pm 18$ | 17 | $60 \pm 15$ | 17 | $65 \pm 13$ | 17 | $64 \pm 14$ | 17 |
| log $g$ (dex) | $5.22 \pm 0.22$ | 16 | $5.12 \pm 0.24$ | 17 | $5.16 \pm 0.2$ | 17 | $5.18 \pm 0.16$ | 17 | $5.18 \pm 0.17$ | 17 |
| Age (Gyr) | 0.5–10 | 16 | 0.5–10 | 17 | 0.5–10 | 17 | 0.5–10 | 17 | 0.5–10 | 17 |
| Distance (**pc**) | $9.3 \pm 0.3$ | 16 | $20.0 \pm 0.6$ | 17 | $12.73 \pm 0.09$ | 17 | $17.0 \pm 0.1$ | 17 | $33.41 \pm 0.06$ | 17 |
| **Retrieved Parameters**[a][b] | | | | | | | | | | |
| $L_{\rm bol}$ | $-4.22 \pm 0.01$ | 17 | $-4.35 \pm 0.01$ | 17 | $-4.21 \pm 0.01$ | 17 | $-3.94 \pm 0.01$ | 17 | $-4.05 \pm 0.01$ | 17 |
| $T_{\rm eff}$ (K) | $1892.31^{+34.48}_{-39.26}$ | 17 | $1708.33^{+20.12}_{-19.82}$ | 17 | $1859.57^{+36.00}_{-33.52}$ | 17 | $1926.13^{+29.87}_{-32.44}$ | 17 | $1920.49^{+27.88}_{-27.93}$ | 17 |
| Radius ($R_{\rm Jup}$) | $0.7^{+0.4}_{-0.3}$ | 17 | $0.74 \pm 0.06$ | 17 | $0.74 \pm 0.04$ | 17 | $0.93 \pm 0.04$ | 17 | $0.83 \pm 0.04$ | 17 |
| Mass ($M_{\rm Jup}$) | $36.36^{+28.4}_{-19.0}$ | 17 | $76.57^{+20.21}_{-25.24}$ | 17 | $34.15^{+30.74}_{-18.19}$ | 17 | $53.98^{+31.69}_{-24.79}$ | 17 | $43.96^{+34.62}_{-23.24}$ | 17 |
| log $g$ (dex) | $5.25^{+0.27}_{-0.35}$ | 17 | $5.55^{+0.07}_{-0.18}$ | 17 | $5.20^{+0.29}_{-0.36}$ | 17 | $5.19^{+0.21}_{-0.28}$ | 17 | $5.20^{+0.26}_{-0.34}$ | 17 |
| C/O[c] | $0.62^{+0.08}_{-0.10}$ | 17 | $0.74 \pm 0.04$ | 17 | $0.71^{+0.07}_{-0.05}$ | 17 | $0.63^{+0.08}_{-0.10}$ | 17 | $0.80 \pm 0.05$ | 17 |
| [M/H][d] | $-0.16^{+0.17}_{-0.19}$ | 17 | $0.34^{+0.12}_{-0.11}$ | 17 | $0.11^{+0.16}_{-0.15}$ | 17 | $-0.08^{+0.14}_{-0.17}$ | 17 | $0.44 \pm 0.18$ | 17 |

**Notes.** In our retrieval models, the distances and corresponding uncertainties are scaled to 10 pc. Therefore we set the distance to the following J1416+1348A:$10 \pm 0.58$, J1526+2043:$10 \pm 0.6$, J0539−0059:$10 \pm 0.09$, J1539−0520:$10 \pm 0.12$, GD 165B:$10 \pm 0.02$.

[a] $L_{\rm bol}$, $T_{\rm eff}$, the radius, the mass, and [M/H] are not directly retrieved parameters but are calculated using the retrieved $R^2/D^2$ and log $g$ values along with the predicted spectrum.

[b] Values are shown for the "winning" models. SDSS J1416+1348A: Power-law deck-cloud, uniform-with-altitude gas abundances. J1526+2043: Cloud-free, uniform-with-altitude gas abundances. For both J0536−0059 and J1539−0520 the power-law deck-cloud, uniform-with-altitude gas abundances and cloud-free, uniform-with-altitude gas abundances models were indistinguishable. We list values for the cloudy model as it has the higher maximum likelihood. See Table 4 for cloudless model values. GD 165B: Power-law deck-cloud, uniform-with-altitude gas abundances.

[c] Absolute inferred atmospheric C/O calculated using $H_2O$, CO, and VO abundances. Solar C/O = 0.55.

[d] Inferred metallicity determined using $H_2O$, CO, VO, CrH, FeH, and Na+K abundances. Values are relative to Solar.

**References:** (1) Burningham et al. (2010), (2) Kirkpatrick et al. (2000), (3) Fan et al. (2000), (4) Kirkpatrick et al. (2008), (5) Kirkpatrick et al. (1999), (6) Bowler et al. (2010), (7) Schneider et al. (2014), (8) Geballe et al. (2002), (9) Kendall et al. (2004), (10) Cutri et al. (2003), (11) Gaia Collaboration et al. (2016),GaiaDR2,Lind18, (12) Blake et al. (2010), (13) Mohanty & Basri (2003), (14) Schmidt et al. (2010), (15) Prato et al. (2015), (16) Gonzales et al. (2020), (17) this Paper.

unusually blue NIR color and determined it to be a member of the thin/thick disk population. Optical and NIR spectra are available for J1539−0520 (Reid et al. 2008; Bardalez Gagliuffi et al. 2014). The available photometry covers the optical, NIR, and MIR wavelengths; see Table 6. The radial velocity and $v\sin i$ were measured in Blake et al. (2010) and are listed in Table 1. The fundamental parameters for J1539−0520 were initially derived in Filippazzo et al. (2015) and are updated here using the same method.

J1539−0520 was tested for *I*-band linear polarization in Zapatero Osorio et al. (2005) but no significant evidence of polarization was found. In Koen (2013), *I*-band photometry of J1539−0520 was found to have large changes in its nightly mean magnitude, which could be evidence of longer-scale variability. However, in the *R* band, they found the magnitude to be consistent or at least less variable. They also noted no evidence for short-timescale variability. Miles-Páez et al. (2017) reported J1539−0520 as an *I*-band variable source with periodic patterns easily seen by eye in the light curve. The variability was posed to be most likely due to rotation causing an inhomogeneous atmosphere. Miles-Páez et al. (2017) determined a rotation period of $2.51^{+1.60}_{-0.55}$ hr and a rotational velocity between 26 and $65 \, \mathrm{km \, s^{-1}}$. With the rotational velocity and observed $v\sin i$ being nearly equal, Miles-Páez et al. (2017) argued it implied J1539−0520 is seen face on. Parameter values for J1539−0520 are listed in Table 1.

### 2.5. GD 165B, $T_{eff}$ Comparison

GD 165B (also known as 2MASS J14243909+0917104) was the first L dwarf discovered (Becklin & Zuckerman 1988) and is a wide spatially resolved companion to the 1.2–5.5 Gyr white dwarf GD 165A (Kirkpatrick et al. 1999). GD 165B has an optical spectral type of L4 and a NIR spectral type of L3 (Kirkpatrick et al. 1999; Geballe et al. 2002). It has numerous optical spectra (R–C Spec: Kirkpatrick et al. 1993; LRIS: Kirkpatrick et al. 1999; HIRES: Mohanty & Basri 2003) and NIR spectra (SpeX prism: Bardalez Gagliuffi et al. 2014; NIRSPEC: McLean et al. 2007; Prato et al. 2015; Martin et al. 2017) as well as photometric measurements listed in Table 6. Astrometric measurements of GD 165B include the parallax (Tinney et al. 1995; van Altena et al. 1995; Gaia Collaboration et al. 2016, 2018; Lindegren et al. 2018), tangential velocity (Tinney et al. 1995), radial velocity (Prato et al. 2015), and $v\sin i$ (Mohanty & Basri 2003). The most precise values of these are listed in Table 1. The fundamental parameters for GD 165B are derived in Leggett et al. (2002) and Filippazzo et al. (2015). We update them in this work using the Filippazzo et al. (2015) method.

### 3. Fundamental Parameters and Overall SED Comparison of the Sample

We used the SED for J1416+1348A from Gonzales et al. (2020) and for each comparative object generated their SEDs using the Filippazzo et al. (2015) method (and code SEDkit),[8] which we briefly discuss below for our targets. For each comparative source except GD 165B, as we only have its NIR data, the optical and NIR spectra (and MIR when available) were combined into a composite spectrum, with the average

spectra taken in regions of overlap. In regions with no overlap, linear interpolation was used to connect the spectra. The composite spectrum was then scaled to the absolute magnitudes of the observed photometry (see Filippazzo et al. 2015 Section 4.2 for details). $L_{\mathrm{bol}}$ was determined by integrating under the distance-calibrated SED from 0 to $1000 \, \mu m$. As done in Filippazzo et al. (2015), to obtain a radius estimate and $T_{\mathrm{eff}}$, we used Saumon & Marley (2008) hybrid cloud evolutionary models as well as the Chabrier et al. (2000) and Saumon & Marley (2008) $f_{\mathrm{sed}} = 2$ evolutionary models to determine the radius ranges for all comparative sources. Additionally due to the later spectral type of J1526+2043, the Baraffe et al. (2003) and cloud-free Saumon & Marley (2008) evolutionary models were also used as done in Filippazzo et al. (2015). The final radius range was then set as the maximum and minimum from all model predictions. For all models we used an age range of 0.5–10 Gyr, corresponding to the field ultracool dwarf age range (Filippazzo et al. 2015). The $T_{\mathrm{eff}}$ was calculated using the Stefan–Boltzmann law along with the inferred radius and calculated $L_{\mathrm{bol}}$. The range of masses was determined using the same evolutionary models used to determine the radius. The photometry and spectra used in the creation of the SEDs are listed in the Appendix, and the fundamental parameters we derive are in Table 1.

The SEDs of the comparative sample along with J1416 +1348A across 0.45–16 $\mu m$ are shown in Figure 1. The SED of J1539−0520 is overluminous across all wavelengths when compared to J1416+1348A. For the $T_{\mathrm{eff}}$ comparisons except J1539−0520, we see that they overlap with one another and J1416+1348A in the optical, while they have a large spread in flux "fanning out" in the NIR. This is derived from the differences in L-dwarf spectra, where the optical spectral type classification is anchored by $T_{\mathrm{eff}}$ with the NIR showing diversity from the secondary parameters (Cruz et al. 2018). As discussed in Zhang et al. (2017) and Gonzales et al. (2018), subdwarfs have effective temperatures similar to those of objects 2–3 spectral types earlier, and thus J1416+1348A agrees well in the optical to the $T_{\mathrm{eff}}$ comparisons due to this. We find that J0539−0059, the coolest $T_{\mathrm{eff}}$ comparison, most closely matches the overall shape of J1416+1348A from the optical through mid *H* band. GD 165B is a close match to J1416+1348A from ∼ 0.85–1.33 $\mu m$, but beyond it is overluminous. In the *K* band and beyond, J1416A more closely shares similarities to the optical spectral type comparison J1526+2043.

It should be noted that, as J1539−0520 is a known variable source, this SED does not represent a consistent picture of the atmosphere at a single point in time, as the data have been taken on different dates. This could also be true for J0539 −0059 as it may be variable. As a test to see if variations on the order of 20% make a difference in the fundamental parameters, adding/subtracting the photometric uncertainty in each band to the measured photometry would produce a variation near this level. From this we find that all fundamental parameters remain within the uncertainties; thus variability at this level should not affect the derived fundamental parameters.

### 4. The *Brewster* Retrieval Framework

Our retrievals use the *Brewster* framework (Burningham et al. 2017) with a modified setup similar to that of Gonzales et al. (2020). The *Brewster* framework is described in extensive detail in Burningham et al. (2017), Gonzales et al. (2020), and

---

[8] SEDkit is available on GitHub at https://github.com/hover2pi/SEDkit. The Eileen branch was used for this work (also available at https://github.com/ECGonzales/SEDkit/tree/master).
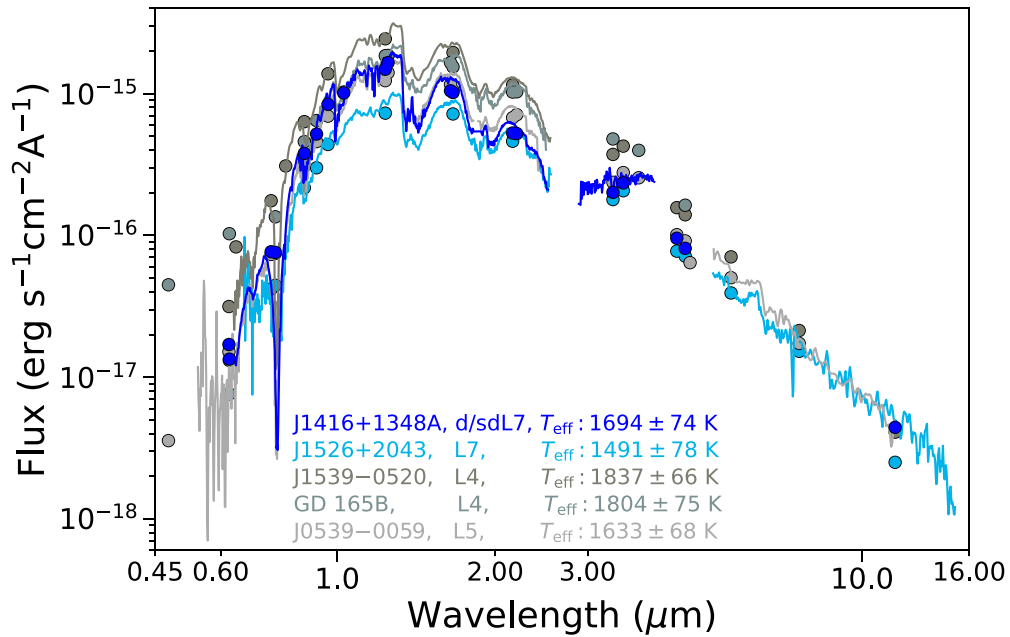
**Figure 1.** Distance-calibrated SEDs of J1416+1348A (dark blue) and comparative sources of similar $T_{\rm eff}$ (J0539−0059, GD 165B, and J1539−0520 in grays) and of the same optical spectral type (J1526+2043 in light blue). All spectra were resampled to the same dispersion relation using a wavelength-dependent Gaussian convolution. The spectra are flux calibrated and scaled to the absolute magnitudes of the photometry shown. No normalization is applied.

Gonzales et al. (2021). Below we briefly describe the key components of the *Brewster* framework and our modifications for this work.

As done in Gonzales et al. (2020), we use the same forward model with the Madhusudhan & Seager (2009) five-parameter P-T profile, gas opacities (only using the Allard opacities for the alkalies), both the uniform-with-altitude and thermochemical equilibrium methods for determining gas abundances, and the same cloud models. The cloud model has the option of either a "slab" or "deck" cloud. Both clouds are defined with the opacity distributed over pressure layers with the optical depth as either gray or a power law ($\tau = \tau_0 \lambda^\alpha$, where $\tau_0$ is the optical depth at $1\,\mu$m). The deck cloud is defined to be optically thick at some pressure level such that the vertical extent of the cloud at lower pressures can only be seen. Three parameters define the deck cloud: (1) the cloud top pressure $P_{\rm top}$, the point at which the cloud passes $\tau = 1$ (looking down), (2) the decay height, $\Delta \log P$, over which the optical depth falls to lower pressures as $d\tau/dP \propto \exp((P - P_{\rm deck})/\Phi)$ where $\Phi = (P_{\rm top}(10^{\Delta \log P} - 1))/(10^{\Delta \log P})$, and (3) the cloud particle single-scattering albedo, which as done in Gonzales et al. (2020) is set to zero, thereby assuming an absorbing cloud. Unlike the deck cloud, the slab cloud is defined in the pressure space to have a top and bottom. Therefore, an additional parameter is included determining the total optical depth at $1\,\mu$m ($\tau_{\rm cloud}$), which is distributed through the slab cloud extent as $d\tau/dP \propto P$ (looking down), reaching its total value at the bottom (highest pressure) of the slab. If the deck or slab cloud has an nongray opacity, an additional parameter for the power ($\alpha$) in the optical depth is included. For additional details on the cloud model see Gonzales et al. (2020), Gonzales et al. (2021), and Section 4.4. The same thermochemical grids are used as in Gonzales et al. (2020), which were calculated using the NASA Gibbs minimization CEA code (McBride & Gordon 1994), based on previous thermochemical models (Fegley & Lodders 1994, 1996; Lodders 1999, 2002, 2010;

Lodders & Fegley 2002, 2006; Visscher et al. 2006, 2010; Moses et al. 2012, 2013; Visscher 2012) and recently utilized to explore gas and condensate chemistry over a range of conditions in substellar atmospheres (Morley et al. 2012, 2013; Kataria et al. 2016; Skemer et al. 2016; Wakeford et al. 2017; Gonzales et al. 2020; Burningham et al. 2021; Gharib-Nezhad et al. 2021; Gonzales et al. 2021; Karalidi et al. 2021; Marley et al. 2021). The chemical grids in this work determine equilibrium abundances of atmospheric species over temperatures between 300 and 4000 K, pressures between 1 $\mu$bar to 300 bar, metallicities ranging from $-1.0 < $ [Fe/H] $ < +2.0$, and C/O abundance ratios of 0.25–2.5x the solar abundance.

### 4.1. Retrieval Model

Our retrieval model uses the EMCEE package (Foreman-Mackey et al. 2013) to sample posterior probabilities with the priors shown in Table 2. As done in Gonzales et al. (2020), for all objects in the sample we extend the mass and temperature priors to allow for surface gravities that encompass the possible ranges for subdwarfs. Distance-calibrated SpeX prism spectra (output from generating our SED) are trimmed to 1.0–2.5 $\mu$m to remove the 0.8–1.0 $\mu$m region of the spectrum impacted by the pressure bordering from the 0.77 $\mu$m K I doublet and set the distance to 10 pc with the correspondingly scaled uncertainty for our retrieval as done in Gonzales et al. (2020).

In each model for the gases, surface gravity, $\Delta\lambda$ (the wavelength shift between the model and data), the scale factor ($R^2/D^2$), cloud top pressure, and power-law parameters we initialize 16 walkers per parameter in a tight Gaussian. The gases are centered around the approximate solar composition equilibrium chemistry values for the gas volume mixing ratios. The surface gravity is initialized centered around the SED-derived value. For our tolerance parameter, optical depth, and cloud thickness we use a flat distribution. Our thermal profile is initialized using the Saumon & Marley (2008) $T_{\rm eff} = 1700$ K $\log g = 5.0$ model. To be sure of convergence, each model is

**Table 2**
Priors for Retrieval Models

| Parameter | Prior |
|---|---|
| gas volume mixing ratio | uniform, $\log f_{gas} \geqslant -12.0$, $\sum_{gas} f_{gas} \leqslant 1.0$ |
| thermal profile ($\alpha_1$, $\alpha_2$, $P1$, $P3$, $T3$) | uniform, $0.0\ \text{K} < T < 6000.0\ \text{K}$ |
| scale factor ($R^2/D^2$) | uniform, $0.5\ R_{Jup} \leqslant R \leqslant 2.0\ R_{Jup}$ |
| gravity ($\log g$) | uniform, $1\ M_{Jup} \leqslant gR^2/G \leqslant 100\ M_{Jup}$ |
| cloud top[a] | uniform, $-4 \leqslant \log P_{CT} \leqslant 2.3$ |
| cloud decay scale[b] | uniform, $0 < \log \Delta P_{decay} < 7$ |
| cloud thickness[c] | uniform, $\log P_{CT} \leqslant \log (P_{CT} + \Delta P) \leqslant 2.3$ |
| cloud total optical depth at $1\mu m$ | uniform, $0.0 \geqslant \tau_{cloud} \geqslant 100.0$ |
| wavelength shift | uniform, $-0.01 < \Delta\lambda < 0.01\mu m$ |
| tolerance factor | uniform, $\log(0.01 \times \min(\sigma_i^2)) \leqslant b \leqslant$ $\log(100 \times max(\sigma_i^2))$ |

**Notes.**
[a] For the deck cloud this is the pressure where $\tau_{cloud} = 1$, for a slab cloud this is the top of the slab.
[b] Decay height for deck cloud above the $\tau_{cloud} = 1.0$ level.
[c] Thickness and $\tau_{cloud}$ only retrieved for slab cloud.

run for at least 50 times the autocorrelation length with the EMCEE chain having 90,000-120,000 iterations. Additionally, we examine the maximum likelihood to ensure that it is no longer fluctuating.

Initially, as done in Gonzales et al. (2020), we retrieved abundances for the following gases: $H_2O$, CO, $CO_2$, $CH_4$, TiO, VO, CrH, FeH, K, and Na, with K and Na tied together as a single element in the state-vector assuming a solar ratio taken from Asplund et al. (2009). However, due to the wavelength coverage and temperatures of the sources, we were unable to constrain $CO_2$, $CH_4$, and TiO for all objects in our sample. For these sources, $CO_2$ and $CH_4$ are not visible in the NIR spectrum but do play a role at longer wavelengths. However, the abundances we retrieve when including $CO_2$, $CH_4$, and TiO the abundances push up against our lower prior bounds and are on the order of $10^{-7.8}$ (for $CO_2$ and $CH_4$) and less than $10^{-9.8}$ (for TiO), much lower than the bounds of primary gases $H_2O$ and CO. Without these species, we can still get meaningful results with only a minor change in our abundances of FeH and CrH. Therefore we removed the unconstrained gases and ran models only including $H_2O$, CO, VO, CrH, FeH, K, and Na, which are reported here. Our retrieval model also includes $H^-$ bound-free and free–free continuum opacities to account for the possibility of the profile going above 3000 K in the photosphere and are set based on the temperature and pulled from the thermochemical equilibrium grids. We test various cloud parameterizations by building up from the cloudless model to the four-parameter power-law slab-cloud model and test the uniform-with-altitude and thermochemical equilibrium gas abundance methods for all cloud models.

## 5. Updating the J1416+1348A Retrieval

By removing the unconstrained gases from our retrieval models for J1416+1348A, we were able to break the degeneracy between the two indistinguishable models in Gonzales et al. (2020)—the power-law deck-cloud model and the power-law slab-cloud model. With $CO_2$, $CH_4$, and TiO removed, the power-law deck-cloud model became strongly preferred over the slab-cloud model for J1416+1348A. We

also find the median P-T profile for the deck-cloud model has shifted to become warmer at slightly lower pressures in the photosphere and deeper compared to the Gonzales et al. (2020) P-T profile, now agreeing more closely with the Sonora (Marley et al. 2021) model grids (see Figure 2(c)). All retrieved gas abundances and derived fundamental parameters for the updated deck-cloud model are consistent with those in Gonzales et al. (2020), as the $1\sigma$ P-T profiles are nearly identical to those in Gonzales et al. (2020). Figures for this updated model can be found on Zenodo.[9]

## 6. Model Selection

Our retrieval models aimed to test which cloud parameterization and gas abundance method is preferred for each of the comparative objects. We explore the nature of clouds in our objects by building up from the least complex cloudless model to the most complex slab-cloud model. For every cloud model, we tested the impact of the uniform-with-altitude and the thermochemical equilibrium gas abundance methods. To rank our models we used the Bayesian information criterion (BIC), where the lowest BIC is preferred. We use the following intervals from Kass & Raftery (1995) for selecting between two models, with evidence against the higher BIC as:

$0 < \Delta\ \text{BIC} < 2$: no preference worth mentioning;
$2 < \Delta\ \text{BIC} < 6$: positive;
$6 < \Delta\ \text{BIC} < 10$: strong;
$10 < \Delta\ \text{BIC}$: very strong.

## 7. Retrieval Results

Table 3 shows all models tested for our comparative sample with their corresponding $\Delta$BIC values. J1416+1348A is best fit by a power-law deck cloud when removing the unconstrained gases from the Gonzales et al. (2020) retrieval. The spectral type comparison, J1526+2043, is best fit by a cloud-free model. Two of the temperature comparisons, J0539−0059 and J1539−0520, however have two indistinguishable best-fit models, a cloud-free model, and a power-law deck-cloud model. While the temperature comparison GD 165B is best fit by a power-law deck-cloud model. The implications of this cloud model degeneracy will be discussed in detail in Section 8.2. Additional figures for each comparative source's "winning" model(s) can be found on Zenodo.[10]

The retrieved and derived parameters for the cloud-free and power-law deck-cloud models of each object can be found in Table 4. The derived radius is determined from the parallax value and the retrieved scale factor ($R^2/D^2$). We then calculate the mass using the derived radius and the retrieved $\log g$. $T_{eff}$ is determined using the radius and integrating the flux in the resultant forward-model spectrum across 0.7–20 $\mu$m. Lastly, we derive the atmospheric metallicity using the following equations:

$$f_{H_2} = 0.84(1 - f_{gases}), \quad (1)$$

$$N_H = 2f_{H_2}N_{tot}, \quad (2)$$

$$N_{element} = \sum_{molecules} n_{atom} f_{molecule} N_{tot}, \quad (3)$$

---

9  https://doi.org/10.5281/zenodo.7045012
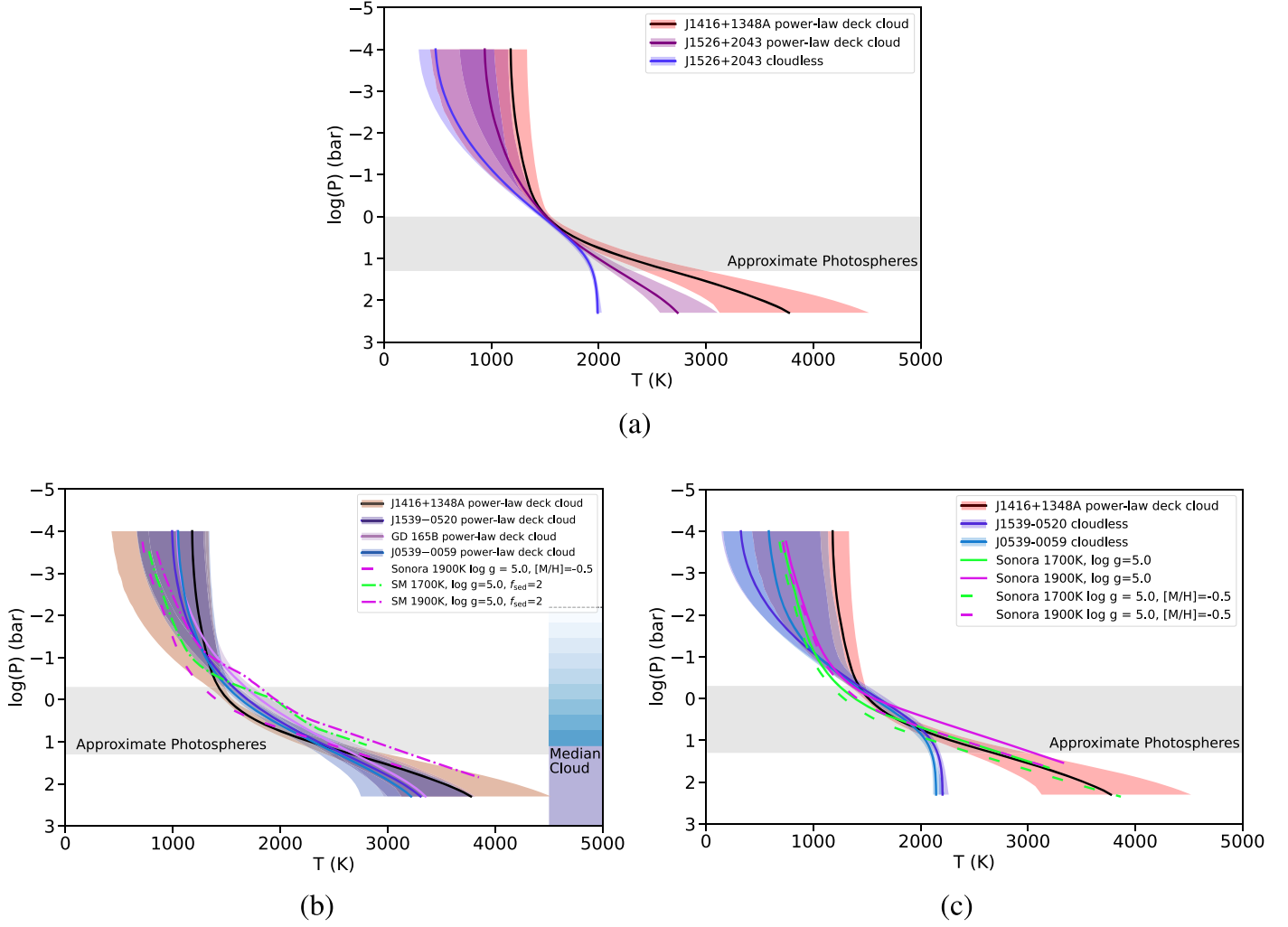10  https://doi.org/10.5281/zenodo.7045012

(a)



(b)



(c)

**Figure 2.** Retrieved P-T profiles of the sample. For each P-T profile, the solid line indicates the median while the shaded region indicates the $1\sigma$ confidence interval. The gray bar indicates the approximate range of the photosphere for the comparison sample. (a) Spectral type comparison P-T profiles: J1526+2043 (purples) and J1416+1348A (black and red). While the cloudless model is the best fit for J1526+2043, we show the power-law deck-cloud model for comparison. (b) $T_{\rm eff}$ comparison cloudy models: J1539−0502 (purple), GD 165B (pink), and J0539−0059 (blue) compared to J1416+1348A (black and red). Overplotted are the Sonora low-metallicity, log $g$ = 5.0 (dotted) model profile (Marley et al. 2021) and the Saumon & Marley (2008) $f_{\rm sed}$ = 2, log $g$ = 5.0 (dotted–dashed) model profiles, which bracket the SED-derived and retrieval-derived effective temperatures (neon green and purple). The far right shows the location of the median cloud top (in purple, where the cloud is optically thick at $\tau = 1$) and vertical distribution of the cloud (in blue shading, showing up to dashed line where the opacity drops to $\tau = 0.5$) for J1416+1348A as a guide. The clouds for all comparative objects are in a similar location. (c) $T_{\rm eff}$ comparison cloudless models: J1539−0520 (purple) and J0539−0059 (blue) compared to J1416+1348A in black and red. Overplotted are the Sonora solar (solid) and low-metallicity (dashed) model profiles, which bracket the SED-derived and retrieval-derived effective temperatures (neon green and purple).

**Table 3**
Retrieval Models of the Comparison Sample

| Model | | N Params | ΔBIC | | | | |
|---|---|---|---|---|---|---|---|
| Cloud Case | Gas Method[a] | | J1416+1348A | J1526+2043 | J0539−0059 | J1539−0520 | GD 165B |
| Cloud Free | uniform | 15 | ⋯ | **0** | **0** | **0** | 3 |
| Gray Deck | uniform | 18 | ⋯ | 19 | 9 | 11.9 | 18 |
| Power-law Deck | uniform | 19 | **0** | 17 | **2** | **0.4** | **0** |
| Gray Slab | uniform | 19 | ⋯ | 21 | 12 | 18.7 | 23 |
| Power-law Slab | uniform | 20 | 5 | 14 | 12 | 7.7 | 8 |
| Cloud Free | CE | 11 | ⋯ | 12 | 36 | 25.7 | 8 |
| Gray Deck | CE | 14 | ⋯ | 4 | 40 | 39.0 | 9 |
| Power-law Deck | CE | 15 | ⋯ | 6 | 5 | 27.1 | 17 |
| Gray Slab | CE | 15 | ⋯ | 10 | 12 | 31.1 | 15 |
| Power-law Slab | CE | 16 | ⋯ | 11 | 13 | 24.1 | 22 |

**Note.** Winning model BIC in bold for ease.
[a] Method used to determine gas abundances. uniform = uniform-with-altitude mixing, CE = chemical equilibrium.

**Table 4**
Retrieved Gas Abundances and Derived Properties for the Comparison Sample

| | SpT Comp | | | | $T_{\rm eff}$ Comp | | | | | |
| | J1416+1348A (d/sdL7) | | J1526+2043 (L7) | | J0539−0059 (L5) | | J1539−0520 (L4) | | GD 165B (L4) | |
| Property | Cloud | Cloud-free | Cloud | Cloud-free | Cloud | Cloud-free | Cloud | Cloud-free | Cloud | Cloud-free |
|---|---|---|---|---|---|---|---|---|---|---|
| | | | | Retrieved | | | | | | |
| $H_2O$ | $-3.67^{+0.12}_{-0.15}$ | ⋯ | $-3.38^{+0.07}_{-0.10}$ | $-3.37^{+0.06}_{-0.09}$ | $-3.56^{+0.15}_{-0.20}$ | $-3.54^{+0.13}_{-0.17}$ | $-3.59^{+0.10}_{-0.15}$ | $-3.67^{+0.10}_{-0.12}$ | $-3.37^{+0.15}_{-0.20}$ | $-3.35^{+0.12}_{-0.16}$ |
| CO | $-3.45^{+0.20}_{-0.22}$ | ⋯ | $-2.92^{+0.09}_{-0.12}$ | $-2.92 \pm 0.12$ | $-3.15^{+0.16}_{-0.17}$ | $-3.16 \pm 0.21$ | $-3.38^{+0.17}_{-0.20}$ | $-3.42^{+0.20}_{-0.21}$ | $-2.79^{+0.18}_{-0.19}$ | $-2.70^{+0.20}_{-0.18}$ |
| VO | $-9.31^{+0.26}_{-0.33}$ | ⋯ | $-9.57^{+0.53}_{-1.43}$ | $-9.19^{+0.30}_{-1.03}$ | $-9.17^{+0.31}_{-0.69}$ | $-8.93^{+0.22}_{-0.27}$ | $-8.86^{+0.19}_{-0.23}$ | $-8.81^{+0.16}_{-0.19}$ | $-8.63^{+0.28}_{-0.40}$ | $-8.33^{+0.21}_{-0.24}$ |
| CrH | $-8.41^{+0.18}_{-0.17}$ | ⋯ | $-8.38^{+0.23}_{-0.29}$ | $-8.13^{+0.19}_{-0.22}$ | $-8.16^{+0.26}_{-0.20}$ | $-8.00^{+0.20}_{-0.22}$ | $-8.00 \pm 0.15$ | $-7.95 \pm 0.16$ | $-7.70^{+0.24}_{-0.28}$ | $-7.43^{+0.23}_{-0.28}$ |
| FeH | $-8.30^{+0.16}_{-0.18}$ | ⋯ | $-8.40^{+0.14}_{-0.18}$ | $-8.83^{+0.23}_{-1.18}$ | $-8.16^{+0.16}_{-0.19}$ | $-8.40^{+0.15}_{-0.24}$ | $-8.11^{+0.12}_{-0.15}$ | $-8.36^{+0.12}_{-0.18}$ | $-7.96^{+0.19}_{-0.28}$ | $-8.30^{+0.19}_{-0.26}$ |
| Na+K | $-6.34^{+0.13}_{-0.21}$ | ⋯ | $-5.63^{+0.18}_{-0.24}$ | $-5.43 \pm 0.19$ | $-5.86^{+0.19}_{-0.25}$ | $-5.67^{+0.20}_{-0.21}$ | $-6.08^{+0.17}_{-0.31}$ | $-5.96^{+0.20}_{-0.31}$ | $-5.64^{+0.34}_{-0.85}$ | $-5.20^{+0.31}_{-0.58}$ |
| log $g$ (dex) | $5.25^{+0.27}_{-0.35}$ | ⋯ | $5.50^{+0.13}_{-0.23}$ | $5.55^{+0.07}_{-0.18}$ | $5.20^{+0.29}_{-0.36}$ | $5.27^{+0.26}_{-0.35}$ | $5.19^{+0.21}_{-0.28}$ | $5.17^{+0.17}_{-0.29}$ | $5.20^{+0.26}_{-0.34}$ | $5.31^{+0.13}_{-0.25}$ |
| | | | | Derived | | | | | | |
| $L_{\rm bol}$ | $-4.22 \pm 0.01$ | ⋯ | $-4.34 \pm 0.01$ | $-4.35 \pm 0.01$ | $-4.21 \pm 0.01$ | $-4.21 \pm 0.01$ | $-3.94 \pm 0.01$ | $-3.94 \pm 0.01$ | $-4.05 \pm 0.01$ | $-4.04 \pm 0.01$ |
| $T_{\rm eff}$ (K) | $1892.31^{+34.48}_{-39.26}$ | ⋯ | $1719.64^{+23.42}_{-21.22}$ | $1708.33^{+20.12}_{-19.82}$ | $1859.57^{+36.00}_{-33.52}$ | $1807.83^{+27.57}_{-25.18}$ | $1926.13^{+29.87}_{-32.44}$ | $1853.87^{+27.86}_{-24.38}$ | $1920.49^{+27.88}_{-27.93}$ | $1842.78^{+27.16}_{-27.55}$ |
| Radius ($R_{\rm Jup}$) | $0.70^{+0.04}_{-0.03}$ | ⋯ | $0.74 \pm 0.06$ | $0.74 \pm 0.06$ | $0.74 \pm 0.04$ | $0.78 \pm 0.03$ | $0.93 \pm 0.04$ | $1.01 \pm 0.04.$ | $0.83 \pm 0.04$ | $0.91 \pm 0.04$ |
| Mass ($M_{\rm Jup}$) | $36.36^{+28.40}_{-19.00}$ | ⋯ | $66.80^{+24.49}_{-25.40}$ | $76.57^{+20.21}_{-25.24}$ | $34.15^{+30.74}_{-18.19}$ | $45.08^{+37.60}_{-23.87}$ | $53.98^{+31.69}_{-24.79}$ | $60.62^{+26.99}_{-28.73}$ | $43.96^{+34.62}_{-23.24}$ | $68.32^{+22.59}_{-29.73}$ |
| C/O[a] | $0.62^{+0.08}_{-0.10}$ | ⋯ | $0.75^{+0.03}_{-0.04}$ | $0.74 \pm 0.04$ | $0.71^{+0.07}_{-0.05}$ | $0.71 \pm 0.06$ | $0.63^{+0.08}_{-0.10}$ | $0.64^{+0.08}_{-0.09}$ | $0.80 \pm 0.05$ | $0.82^{+0.04}_{-0.05}$ |
| [M/H][a] | $-0.16^{+0.17}_{-0.19}$ | ⋯ | $0.33^{+0.09}_{-0.11}$ | $0.34^{+0.12}_{-0.11}$ | $0.11^{+0.16}_{-0.15}$ | $0.11^{+0.20}_{-0.18}$ | $-0.08^{+0.14}_{-0.17}$ | $-0.14 \pm 0.17$ | $0.44 \pm 0.18$ | $0.53^{+0.19}_{-0.17}$ |

**Note.** The cloud models are power-law deck-cloud models. The best-fit model for J1526+2043 is the cloud-free model. The cloudy model is shown for comparison. For J0539−0059 and J1539−0502, the cloudy and cloud-free models are indistinguishable. The best-fit model for GD 165B is the cloudy model, with the cloud-free model only shown for comparative purposes. Both the cloudy and cloud-free models have uniform-with-altitude gas abundances. The molecular abundances are fractions listed as log values.
[a] Atmospheric value.

8

$$N_M = \sum_{\text{elements}} \frac{N_{\text{element}}}{N_H}, \qquad (4)$$

where $f_{H_2}$ is the $H_2$ fraction, $f_{\text{gases}}$ is the total gas fraction for all other gases, $N_H$ is the number of neutral hydrogen atoms, $N_{\text{tot}}$ is the total number of gas molecules, $N_{\text{element}}$ is the number of atoms for the element of interest, and $n_{\text{atom}}$ is the number of atoms of that element in a molecule (e.g., two for oxygen in $CO_2$). Thus the final value of [M/H] is

$$[\text{M/H}] = \log \frac{N_M}{N_{\text{Solar}}}, \qquad (5)$$

where $N_{\text{Solar}}$ is calculated as the sum of the solar abundances (from Asplund et al. 2009) relative to H. We do not account for gases that are invisible (e.g., Nitrogen) in our atmospheric metallicity calculation. For all comparative sources we find that the retrieved and derived parameters are consistent between the cloud-free and cloudy models, with the exception of the $T_{\text{eff}}$ for J1539−0520 and GD 165B. Importantly as the C/O ratio and metallicity between both the cloudless and cloudy models are consistent, if the gas abundances and fundamental parameters are only of concern, then one can confidently derive these while using a poorer fitting cloud model for theses sources and likely others if they behave likewise.

Comparing the temperature-comparison objects J0539 −0059, J1539−0520, and GD 165B to J1416+13148A we find that the C/O ratio and metallicity are consistent with the exception of GD 165B. Further, a majority of the retrieved and derived parameters agree with the exception of the alkalies for J0539−0059, CO and VO for GD 165B, and CrH, $L_{\text{bol}}$, and the radius for both J1539−0520 and GD 165B. Of note, the radius we derive for J1539−0520 is much larger than the other objects in this sample.

When comparing the retrieval-based values to the SED-based values (see Table 1), the $T_{\text{eff}}$ of all comparison objects are ∼100–200 K warmer than the semi-empirical $T_{\text{eff}}$ following the trend seen for J1416+13148A in Gonzales et al. (2020) and this work, as well as for the unusually red L dwarf 2MASSW J2224438-015852 (hereafter J2224−0158) in Burningham et al. (2021). For J1416+13148A, J1526+2043, J0539 −0059, and GD 165B, the retrieved radius is smaller than expected from the evolutionary models, which follows the trend seen in previous L-dwarf retrieval works (e.g., Burningham et al. 2017; Gonzales et al. 2020; Burningham et al. 2021). This is also seen in observational AKARI spectra in Sorahana et al. (2013), which used a similar method to ours to estimate the radii. For most of the mid- to late-L dwarfs in their sample they find smaller radii than predicted from evolutionary models in the range of 0.64–0.81 $R_{\text{Jup}}$, which encompasses the radii we find for J1416+13148A, J1526+2043, J0539−0059, and GD 165B. Unlike J1416+13148A and the other comparative objects, the radius values for J1539−0520 agree between the two methods. It is unclear why this object is the only one for which these two methods agree.

## 8. Discussion

### 8.1. Comparing P-T Profiles for Objects of the Same Spectral Type

Figure 2(a) compares the P-T profiles for the power-law deck-cloud models of J1416+1348A and J1526+2043, as well

as the cloudless winning model for J1526+2043. The power-law deck cloud was not the winning model for J1526+2043 (ΔBIC = 17); however to compare it to J1416+1348A we show the same cloud model. An important finding is that the retrieved and derived parameters for J1526+2043 agree within $1\sigma$ between the cloud-free and power-law deck-cloud models (see Table 4). The cloud-free and power-law deck-cloud profiles of J1526+2043 agree within $1\sigma$ until they reach pressures of ∼10 bar. At this point for the cloudy model, the cloud opacity becomes optically thick, and thus we gain no more information below the cloud top for the P-T profile. This is because the shape of the deeper profile is an extrapolation of the profile at lower pressures. For the cloud-free model the turning of the profile to nearly isothermal around 10 bars attempts to recreate the affect of a cloud when one is not present in the model. Therefore because of these affects the retrieved parameters in Table 4 are consistent between these two models.

At pressures below ∼1 bar (higher up in the atmosphere) the profiles for J1416+1348A and J1526+2043 agree within $1\sigma$. However, at ∼1 bar and above (lower down in the atmosphere) J1526+2043 is cooler than J1416+1348A and cools quicker with a steeper profile. While of similar spectral types, J1526 +2043 is nearly 180 K cooler than J1416+1348A. This agrees with previous observational findings for L subdwarfs to be 100–400 K warmer than similar spectral typed field-age L dwarfs (Zhang et al. 2017; Gonzales et al. 2018). P-T profile comparisons are likely better suited to objects of similar $T_{\text{eff}}$ values.

### 8.2. Comparing P-T Profiles for Object of the Same Temperature

The "winning" P-T profiles of the $T_{\text{eff}}$ sample are compared with J1416+1348A in Figures 2(b) and (c), respectively. GD 165B was best fit by a power-law deck-cloud model, while J1539−0502 and J0539−0059 were equally well fit by a cloudless model and a power-law deck-cloud model (see Table 3 for the ΔBIC values). The power-law deck-cloud models of J1539−0502 and J0539−0059, however, have a higher maximum likelihood compared to the cloudless models.

The P-T profiles of $T_{\text{eff}}$ objects generally agree overall to J1416+1348A, much better than the spectral type comparison did (see Figure 2(a)). At pressures below ∼0.1 bar, J1539 −0520, GD 165B, and J0539−0059 agree within $1\sigma$ to J1416 +1348A. For the cloudy and cloudless models in Figure 2(b) and (c), between ∼ 0.5 and 10 bars, the comparative objects are hotter than J1416+1348A. The comparative objects become cooler than J1416+1348A at pressures greater than ∼10 bars.

Overplotted in Figure 2(b) are the 1900 K, [M/H] = − 0.5, log $g$ = 5.0 Sonora (Marley et al. 2021) profile (dotted line) and the Saumon & Marley (2008; SM) $f_{\text{sed}}$ = 2 for temperatures bracketing the semi-empirical and retrieved values. At pressures lower than those of the photosphere (higher altitudes), we see that the median profiles for all objects are hotter and more isothermal than the Sonora and SM grid model profiles. Within the photosphere, J1416+1348A's profile agrees with the Sonora cloudless profile within the $1\sigma$ confidence intervals, while for the comparative objects, the profiles are steeper and cooler than expected from the deep adiabat of the SM profiles. This indicates a missing source of opacity in our current retrieval models for the comparative sources, likely coming from an additional cloud. Figure 3
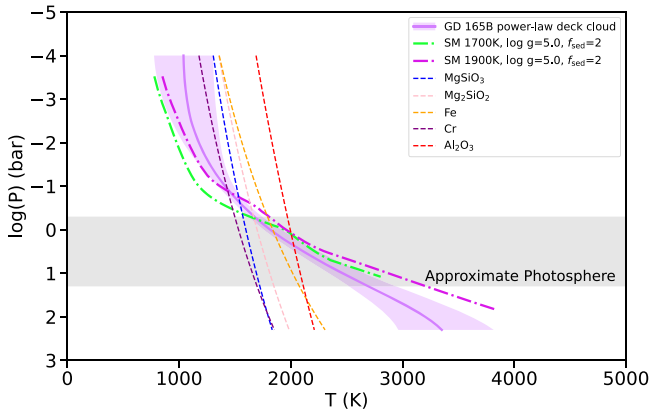
**Figure 3.** Retrieved P-T profile of GD 165B. The gray bar indicates the approximate range of the photosphere. Overplotted are the Saumon & Marley (2008) model profiles that bracket the SED- and retrieval-based $T_{\text{eff}}$ (magenta and neon green dot dashed, respectively), along with various cloud species condensation curves (colored dashed).

shows the P-T profile of GD 165B plotted along with the SM grid models and possible condensation curves for various species for these temperatures. Just above the photosphere, the P-T profile of GD 165B intersects with the ensatite (MgSiO$_3$) and forsterite (Mg$_2$SiO$_4$) condensation curves–two possible additional opacity sources. This has also been seen previously for J2224−0158. When initially retrieved in Burningham et al. (2017), only the NIR data was included resulting in a power-law deck cloud, the same cloud model we have for the $T_{\text{eff}}$ comparatives. In Burningham et al. (2021), when the MIR spectrum was included, which probes higher altitudes than the NIR spectrum, they found that silicate clouds introduced additional opacity sources not visible in the NIR data. As our comparative sources are of similar $T_{\text{eff}}$ to J2224−0158 we expect these opacity sources to likely play a role in their atmospheres as well. It should be also noted that the Sonora and SM grid models include gas opacity sources not included in our model (e.g., CO$_2$ and CH$_4$, which are expected to be the next two most abundant gas species in our atmosphere but do not have spectral features in the NIR at these temperatures. We do not constrain these gases for all objects in this sample and while they play a role in shaping our P-T profile, it is not as strong of an impact as that of missing cloud opacities. This is best displayed by the fact that the removal of these gases had little impact on the shape of J1416+1348A's profile.

One may wonder if the wavelength coverage, S/N, metallicity, or variability play a role in the indistinguishable cloud models for J0539−0059 and J1539−0520 compared to GD 165B, which has a clear preference for the cloudy model. This will be discussed below in Sections 8.3, 8.4, and 8.5.

### 8.3. Does the Wavelength Coverage Impact Degenerate Cloud Models?

To break the degeneracy between the cloudless and cloudy models for J0539−0059 and J1539−0520 we need either (1) a more restricted P-T profile or (2) MIR data that provides additional information about clouds at higher altitudes. By including MIR data, we can get a better handle on the pseudo-continuum (e.g., see Figure 1), which will impact the shape of the P-T profile, as well as additional cloud opacity. While the cloud in the atmosphere of J1416+1348A impacts a small portion of its *J*-band spectrum (see Gonzales et al. 2020,

Figures 2(b) and 7(b) and the contribution function figure on Zenodo), the missing clouds in the atmospheres of the $T_{\text{eff}}$ comparative sources likely impact a larger portion of the spectrum and thus contribute more to the P-T profile shape necessitating either of the suggested solutions to break the degeneracy.

Changes to the shape of the P-T profile have been seen previously in the study of the unusually red L dwarf J2224−0158 in Burningham et al. (2017) and Burningham et al. (2021). Burningham et al. (2017) examined J2224−0158 using NIR data only and found it was best fit by a power-law deck-cloud model with a steeper profile than expected from the Saumon & Marley (2008) grid model profiles deep in the atmosphere. When the MIR data was included in Burningham et al. (2021), the retrieved profile became shallower and thus better matched the expected model profile. Therefore, we expect additional data for J0539−0059 and J1539−0520 to behave in a similar fashion. J0539−0059 currently has MIR Spitzer data, which was not included in this retrieval study as we aim to compare the same wavelength coverage for all objects; however, we are be exploring its impact as part of a study of objects with broad wavelength coverage (E. Gonzales et al. 2022, in preparation). Therefore we stress the connection between the P-T profile shape and the nature of clouds in a substellar atmosphere in the absence of long-wavelength coverage. With a lack of broad wavelength coverage, the P-T profile retrieved can be drastically different than the true shape.

### 8.4. Does Metallicity Impact the P-T Profile Shape?

Metallicity plays a key role in helping shape the pseudo-continuum of a target's spectrum. As shown by the Sonora grid models in Figure 2(c), as the metallicity decreases the "bend" in the P-T profile, the transition between the radiative and convective zones, moves diagonally to the bottom left (see the region within the approximate photosphere). It should also be noted that a change in temperature also impacts the "bend". This metallicity trend is also seen in the comparative objects in Figure 2(b) as they have differing metallicities (see Table 4 for values). While the differing metallicities of the sample impact the region between ∼ 1 and 10 bars, where the sample profiles do not overlap, this likely does not have a major impact on their mismatch with the gird model P-T profile deep adiabatic region because the majority of the $T_{\text{eff}}$ sample is consistent with Solar metallicity. Likely, instead, the major impact is the missing cloud opacity for all three $T_{\text{eff}}$ comparative objects.

### 8.5. How Does the Signal-to-noise Ratio Impact the Ability to Distinguish between Cloud Models and Retrieved Parameter Uncertainties?

The SpeX spectra of the comparison sample provide a range of S/N values for each spectrum retrieved. Therefore we evaluate the impact S/N may play on indistinguishable cloud models or gas abundance uncertainties. Table 5 lists the S/N for each of the objects in the sample across various regions in their NIR spectrum. Comparisons of each spectrum's S/N in the sample demonstrate whether S/N impacts the cloud model choice as well as how tightly the retrieved gas abundances can be constrained.

In particular, J1539−0520 and GD 165B have the same $T_{\text{eff}}$ and spectral types but differ in S/N (J1539−0520 has a higher S/N spectrum). Therefore we can contrast resultant values to

**Table 5**
Signal-to-noise Ratio of the Spectra Used

| Object | Spectral Type | Retrieved $T_{\mathrm{eff}}$ | Top Model | Second Model | Signal-to-noise | | | |
|---|---|---|---|---|---|---|---|---|
| | | | | | YJ | H | J peak | H plateau |
| J1416+1348A | d/sdL7 | $1892.31^{+34.48}_{-39.26}$ | power-law deck-cloud, uniform | power-law slab-cloud, uniform | 341 | 359 | 437 | 423 |
| J1526+2043 | L7 | $1708.33^{+20.12}_{-19.82}$ | cloudless, uniform | gray deck-cloud, CE | 83 | 99 | 95 | 111 |
| J0539−0059 | L5 | $1859.57^{+36.00}_{-33.52}$ | cloudless, uniform[a] | power-law deck-cloud, uniform[a] | 228 | 231 | 302 | 227 |
| J1539−0520 | L4 | $1926.13^{+29.87}_{-32.44}$ | cloudless, uniform[a] | power-law deck-cloud, uniform[a] | 176 | 178 | 219 | 198 |
| GD 165B | L4 | $1920.49^{+27.88}_{-27.93}$ | power-law deck-cloud, uniform | cloudless, uniform | 63 | 67 | 79 | 78 |

**Note.** Uniform = uniform-with-altitude mixing, CE = Chemical Equilibrium. The S/N is calculated between the following wavelengths for *YJ*: 1.0–1.35 μm, *H*: 1.42–1.80 μm, *J* peak: 1.26–1.32 μm, and *H* plateau:1.55–1.70 μm.
[a] Indistinguishable models.

determine the impact S/N may have on scientific conclusions. J1539−0520 is a variable source currently thought to have cloud variability, and thus we need to consider the impact of more than one source of cloud opacity. However, as discussed in Section 8.3, NIR data alone cannot probe enough of the atmosphere to best constrain the cloud properties for J1539 −0520. For GD 165B, while it is best fit by a cloudy model, it too is likely missing additional cloud opacity as the deep adiabat slope of the P-T profile also differs from the expected grid model slope. Another difference in the two sources is their metallicity; however, as discussed in Section 8.4 above, metallicity should impact the relative location of the "bend" in the P-T profile (the transition from the adiabatic region to the radiative region). Looking at Table 5, we can see that S/N does not play a role in constraining the difference between the cloudy and cloudless models. Both J1416+1348A and GD 165B have distinguishable cloud models with S/N values of 437 and 79, respectively, at the *J*-band peak, while J1539 −0520 has a S/N of 219 at the *J*-band peak and cannot differ between the cloudy and cloud-free models. It should be noted that these S/N ratios are relatively high, placing us in a regime where model uncertainties dominate as opposed to data uncertainties. This may not be the case when examining cloud model differences between spectra with S/N $\lesssim$ 50. Therefore, the impact of wavelength coverage plays a more significant role in distinguishing between cloud models than the S/N does when S/N $\gtrsim$ 80. As clouds affect the spectrum over a wide range of wavelengths, there should be no specific features that would require a higher S/N than presented here to be resolved.

One may also ask how S/N impacts the uncertainties for our retrieved parameters. Comparing the retrieved parameters of J1539−0520 and GD 165B, the uncertainties for GD 165B are only slightly larger than those of J1539−0520. Therefore, the S/N could play a minor role in the size of the retrieved parameter uncertainties; however, with a S/N greater than 79 in the *J*-band peak, there appears to be no significant difference in the size of the uncertainties.

*8.6. The Impact of Unconstrained Gases on Model Selection*

When including all of the gases initially used in Gonzales et al. (2020) for the comparative sample, we found that the "winning" model used the thermochemical equilibrium method for J1526+2043 (gray deck cloud) and J0539−0059 (power-law deck cloud). However, once the unconstrained gases were removed, the "winning" models for both J1526+2043 (cloud-free) and J0539−0059 (indistinguishable between the cloudless and power-law deck-cloud models) used the uniform-with-

altitude method, meaning a free retrieval is preferred. By removing the unconstrained gases from our model, we reduced the number of parameters in the uniform-with-altitude retrieval models. These removed "excess" model parameters (those which cannot be constrained based on our data) impact the ΔBIC for the uniform-with-altitude models but not the thermochemical models. While the uniform-with-altitude method is not physically motivated, the flexibility provided by determining individual gas abundances provides a better fit to the data than the thermochemical equilibrium method, which retrieves a C/O ratio and a metallicity instead, and thus is the preferred method once the unconstrained parameters are removed. Burningham et al. (2021), posed that the challenge in accurately modeling the broadened alkali wings could be a physical reason for this preference. Like seen in their work we too are unable to simultaneously fit the pseudo-continuum near 1 μm impacted by the pressure broaden K I 0.77 μm wings and the narrow *J*-band K I lines. Therefore, determining which gases should be included in the retrieval model via iteration is critical for model selection, particularly when deciding between the uniform-with-altitude and thermochemical equilibrium methods.

**9. Conclusions**

Here we present an updated retrieval of J1416+1348A and the first retrievals of J1526+2043, J0539−0059, J1539−0520, and GD 165B to address the question, "How do the P-T profiles of objects of the same spectral type or $T_{\mathrm{eff}}$ compare to one another?". From our retrieval models we find that the P-T profiles of objects of similar $T_{\mathrm{eff}}$ look more similar to one another than objects of the same spectral type. This is critical for subdwarfs as objects of similar spectral type can differ by up to 400 K. We also noted that a mismatch in the slope at ~0.5 bar and deeper (adiabatic region) of our retrieved P-T profiles for J0539−0059, J1539−0520, and GD 165B compared to the expected shape from the Saumon & Marley (2008) grid models. This indicates that our retrieval models are missing an opacity source, which is likely due to an additional cloud. Retrieval model degeneracies will be even more critical for directly imaged exoplanets due to their limited wavelength coverage. To address this, particularly for objects for which we are unable to distinguish between the cloudless and cloudy models, we can either (1) use a more restricted P-T profile on our current data, or (2) include MIR wavelength data as it will allow us to better constrain the pseudo-continuum of our spectrum as well as provide information about cloud opacities at higher altitudes in the atmosphere. Additionally, we noted

that the metallicity of a source does not play a large role in the shape of the P-T profile retrieved, but instead missing cloud opacities have a larger impact. We also note that when the input spectrum S/N is $\gtrsim$80, it does not impact the ability to distinguish between various cloud models, but it could play a minor role in how tightly the retrieved parameters are constrained. Lastly, we highlight the importance of identifying the "minimum complexity" retrieval model, as the addition of unconstrained gases can impact the preference between a uniform-with-altitude gas abundance method and a thermo-chemical equilibrium gas abundance method.

## Appendix
## Data Used For Generating SEDs

Tables 6 and 7 list all the photometry and spectral information used to generate the SEDs of the samples.

**Table 6**
Photometry Used for Comparative sample SEDs

| Band | J1526+2043 | References | J0539−0059 | References | J1539−0520 | References | GD 165B | References |
|---|---|---|---|---|---|---|---|---|
| Pan-STARRS $r$ | ⋯ | ⋯ | 21.076 ± 0.05 | 1 | 20.906 ± 0.06 | 1 | ⋯ | ⋯ |
| Pan-STARRS $i$ | 20.301 ± 0.06 | 1 | 18.711 ± 0.11 | 1 | 18.391 ± 0.01 | 1 | ⋯ | ⋯ |
| Pan-STARRS $z$ | 18.061 ± 0.01 | 1 | 16.651 ± 0.01 | 1 | 16.541 ± 0.01 | 1 | 18.87 ± 0.01 | 1 |
| Pan-STARRS $y$ | 17.039 ± 0.01 | 1 | 15.559 ± 0.01 | 1 | 15.439 ± 0.01 | 1 | ⋯ | ⋯ |
| SDSS $g$ | ⋯ | ⋯ | 23.49 ± 0.27 | 2 | ⋯ | ⋯ | 22.76 ± 0.23 | 2 |
| SDSS $r$ | 22.81 ± 0.23 | 2 | 21.236 ± 0.061 | 2 | ⋯ | ⋯ | 21.255 ± 0.073 | 2 |
| SDSS $i$ | 20.256 ± 0.05 | 2 | 18.713 ± 0.015 | 2 | ⋯ | ⋯ | 20.532 ± 0.055 | 2 |
| SDSS $z$ | 17.635 ± 0.025 | 2 | 16.1929 ± 0.0093 | 2 | ⋯ | ⋯ | 18.456 ± 0.031 | 2 |
| Cousins $R$ | ⋯ | ⋯ | ⋯ | ⋯ | 19.6882 ± 0.035 | 3 | ⋯ | ⋯ |
| Cousins $I$ | ⋯ | ⋯ | ⋯ | ⋯ | 17.5614 ± 0.046 | 3 | ⋯ | ⋯ |
| 2MASS $J$ | 15.586 ± 0.055 | 4 | 14.033 ± 0.031 | 4 | 13.922 ± 0.029 | 4 | 15.687 ± 0.078 | 4 |
| 2MASS $H$ | 14.497 ± 0.044 | 4 | 13.104 ± 0.026 | 4 | 13.06 ± 0.026 | 4 | 14.781 ± 0.07 | 4 |
| 2MASS $K_\mathrm{s}$ | 13.922 ± 0.052 | 4 | 12.527 ± 0.024 | 4 | 12.575 ± 0.029 | 4 | 14.169 ± 0.095 | 4 |
| MKO $Y$ | ⋯ | ⋯ | ⋯ | ⋯ | ⋯ | ⋯ | 17.01 ± 0.1 | 5 |
| MKO $J$ | ⋯ | ⋯ | 13.85 ± 0.03 | 6 | ⋯ | ⋯ | 15.64 ± 0.05 | 7 |
| MKO $H$ | ⋯ | ⋯ | 13.04 ± 0.03 | 6 | ⋯ | ⋯ | 14.75 ± 0.05 | 7 |
| MKO $K$ | ⋯ | ⋯ | 12.4 ± 0.03 | 6 | ⋯ | ⋯ | 14.09 ± 0.05 | 7 |
| MKO $L'$ | ⋯ | ⋯ | 11.32 ± 0.05 | 7 | ⋯ | ⋯ | 12.93 ± 0.07 | 8 |
| MKO $M'$ | ⋯ | ⋯ | 11.87 ± 0.11 | 9 | ⋯ | ⋯ | ⋯ | ⋯ |
| WISE $W1$ | 13.153 ± 0.025 | 10 | 11.869 ± 0.023 | 10 | 12.004 ± 0.023 | 10 | 13.198 ± 0.024 | 10 |
| WISE $W2$ | 12.826 ± 0.025 | 10 | 11.578 ± 0.021 | 10 | 11.744 ± 0.022 | 10 | 13.042 ± 0.026 | 10 |
| WISE $W3$ | 12.54 ± 0.267 | 10 | ⋯ | ⋯ | 11.655 ± 0.23 | 10 | ⋯ | ⋯ |
| IRAC [3.6 $\mu$m] | 12.79 ± 0.02 | 11 | 11.49 ± 0.02 | 11 | 11.65 ± 0.02 | 11 | ⋯ | ⋯ |
| IRAC [4.5 $\mu$m] | 12.87 ± 0.03 | 11 | 11.6 ± 0.02 | 11 | 11.75 ± 0.04 | 11 | ⋯ | ⋯ |
| IRAC [5.8 $\mu$m] | 12.6 ± 0.11 | 11 | 11.35 ± 0.03 | 11 | 11.61 ± 0.05 | 11 | ⋯ | ⋯ |
| IRAC [8.0 $\mu$m] | 12.32 ± 0.04 | 11 | 11.2 ± 0.04 | 11 | 11.6 ± 0.05 | 11 | ⋯ | ⋯ |

**References:** (1) Chambers et al. (2016), (2) Ahn et al. (2012), (3) Dieterich et al. (2014), (4) Cutri et al. (2003), (5) Bardalez Gagliuffi et al. (2014), (6) Leggett et al. (2000), (7) Leggett et al. (2002), (8) Jones et al. (1996), (9) Golimowski et al. (2004), (10) Cutri et al. (2012), (11) Patten et al. (2006).

**Table 7**
Spectra Used to Construct the SEDs

| Name | OPT | OPT Obs. Date | OPT References | NIR | NIR Obs. Date | NIR References | MIR | MIR Obs. Date | MIR References |
|---|---|---|---|---|---|---|---|---|---|
| J1526+2043 | LRIS | 1998 Sep 20 | 1 | SpeX Prism | 2003 May 23 | 2 | IRS | 2006 Jan 17 | 3 |
| J0539−0059 | ARC 3.5 m: DIS | 1999 Mar 20 | 4 | SpeX SXD[a] | 2005 Apr 06 | 5 | IRS | 2006 Jan 17 | 3 |
| J1539−0520 | KPNO 4 m: R–C Spec | 2004 Feb 10 | 6 | SpeX Prism | 2008 Jul 14 | 7 | … | … | … |
| GD 165B | … | … | … | SpeX Prism | 2009 Jun 29 | 7 | … | … | … |

**Notes.** For all retrievals, only the NIR SpeX prism spectra from $1 - 2.5\ \mu m$ were used.
[a] Only SpeX prism spectrum used for retrieval. J0539: 2000 Nov 06, Schneider et al. (2014). J1416A: 2009 Jun 28, Schmidt et al. (2010).
[b] Combined spectrum of observations on 2011–02–05, 2011–02–12, and 2011–04–13.
**References:** (1) Kirkpatrick et al. (2000), (2) Burgasser et al. (2004), (3) Cushing et al. (2006), (4) Fan et al. (2000), (5) Cushing et al. (2005), (6) Reid et al. (2008), (7) Bardalez Gagliuffi et al. (2014).

## ORCID iDs

Eileen C. Gonzales ⓘ https://orcid.org/0000-0003-4636-6676
Ben Burningham ⓘ https://orcid.org/0000-0003-4600-5627
Jacqueline K. Faherty ⓘ https://orcid.org/0000-0001-6251-0573
Nikole K. Lewis ⓘ https://orcid.org/0000-0002-8507-1304
Channon Visscher ⓘ https://orcid.org/0000-0001-6627-6067
Mark Marley ⓘ https://orcid.org/0000-0002-5251-2943

## References

Abazajian, K. N., Adelman-McCarthy, J. K., Agüeros, M. A., et al. 2009, ApJS, 182, 543
Ahn, C. P., Alexandroff, R., Allende Prieto, C., et al. 2012, ApJS, 203, 21
Allers, K. N., & Liu, M. C. 2013, ApJ, 772, 79
Allers, K. N., Liu, M. C., Dupuy, T. J., & Cushing, M. C. 2010, ApJ, 715, 561
Asplund, M., Grevesse, N., Sauval, A. J., & Scott, P. 2009, ARA&A, 47, 481
Astropy Collaboration, Robitaille, T. P., Tollerud, E. J., et al. 2013, A&A, 558, A33
Bailer-Jones, C. A. L. 2008, MNRAS, 384, 1145
Bailer-Jones, C. A. L., & Mundt, R. 2001, A&A, 367, 218
Baraffe, I., Chabrier, G., Barman, T. S., Allard, F., & Hauschildt, P. H. 2003, A&A, 402, 701
Bardalez Gagliuffi, D. C., Burgasser, A. J., Gelino, C. R., et al. 2014, ApJ, 794, 143
Becklin, E. E., & Zuckerman, B. 1988, Natur, 336, 656
Bell, C. P. M., Mamajek, E. E., & Naylor, T. 2015, MNRAS, 454, 593
Blake, C. H., Charbonneau, D., & White, R. J. 2010, ApJ, 723, 684
Bowler, B. P., Liu, M. C., & Dupuy, T. J. 2010, ApJ, 710, 45
Buenzli, E., Apai, D., Radigan, J., Reid, I. N., & Flateau, D. 2014, ApJ, 782, 77
Burgasser, A. J., McElwain, M. W., Kirkpatrick, J. D., et al. 2004, AJ, 127, 2856
Burgasser, A. J., Kirkpatrick, J. D., Brown, M. E., et al. 2002, ApJ, 564, 421
Burgasser, A. J., Kirkpatrick, J. D., Burrows, A., et al. 2003, ApJ, 592, 1186
Burgasser, A. J., Logsdon, S. E., Gagné, J., et al. 2015, ApJS, 220, 18
Burgasser, A. J., Vrba, F. J., Lépine, S., et al. 2008, ApJ, 672, 1159
Burgasser, A. J., Witte, S., Helling, C., et al. 2009, ApJ, 697, 148
Burningham, B., Faherty, J. K., Gonzales, E. C., et al. 2021, MNRAS, 506, 1944
Burningham, B., Leggett, S. K., Lucas, P. W., et al. 2010, MNRAS, 404, 1952
Burningham, B., Marley, M. S., Line, M. R., et al. 2017, MNRAS, 470, 1177
Chabrier, G., & Baraffe, I. 1997, A&A, 327, 1039
Chabrier, G., Baraffe, I., Allard, F., & Hauschildt, P. 2000, ApJ, 542, 464
Chambers, K. C., Magnier, E. A., Metcalfe, N., et al. 2016, arXiv:1612.05560
Cruz, K. L., Kirkpatrick, J. D., & Burgasser, A. J. 2009, AJ, 137, 3345
Cruz, K. L., Núñez, A., Burgasser, A. J., et al. 2018, AJ, 155, 34
Cushing, M. C., Kirkpatrick, J. D., Gelino, C. R., et al. 2011, ApJ, 743, 50
Cushing, M. C., Looper, D., Burgasser, A. J., et al. 2009, ApJ, 696, 986
Cushing, M. C., Rayner, J. T., & Vacca, W. D. 2005, ApJ, 623, 1115
Cushing, M. C., Roellig, T. L., Marley, M. S., et al. 2006, ApJ, 648, 614
Cushing, M. C., Saumon, D., & Marley, M. S. 2010, AJ, 140, 1428
Cutri, R. M., Wright, E. L., Conrow, T., et al. 2012, VizieR On-line Data Catalog: II/311
Cutri, R. M., Skrutskie, M. F., van Dyk, S., et al. 2003, 2MASS All Sky Catalog of Point Sources

Dahn, C. C., Harris, H. C., Levine, S. E., et al. 2008, ApJ, 686, 548
Dieterich, S. B., Henry, T. J., Jao, W.-C., et al. 2014, AJ, 147, 94
Dupuy, T. J., & Liu, M. C. 2017, ApJS, 231, 15
Faherty, J. K., Burgasser, A. J., Cruz, K. L., et al. 2009, AJ, 137, 1
Faherty, J. K., Burgasser, A. J., Walter, F. M., et al. 2012, ApJ, 752, 56
Faherty, J. K., Riedel, A. R., Cruz, K. L., et al. 2016, ApJS, 225, 10
Fan, X., Knapp, G. R., Strauss, M. A., et al. 2000, AJ, 119, 928
Fegley, B., Jr., & Lodders, K. 1994, Icar, 110, 117
Fegley, B., Jr., & Lodders, K. 1996, ApJL, 472, L37
Filippazzo, J. C., Rice, E. L., Faherty, J., et al. 2015, ApJ, 810, 158
Foreman-Mackey, D. 2016, JOSS, 1, 24
Foreman-Mackey, D., Hogg, D. W., Lang, D., & Goodman, J. 2013, PASP, 125, 306
Gagné, J., Faherty, J. K., Burgasser, A. J., et al. 2017, ApJL, 841, L1
Gaia Collaboration, Brown, A. G. A., Vallenari, A., et al. 2016, A&A, 595, A2
Gaia Collaboration, Brown, A. G. A., Vallenari, A., et al. 2018, A&A, 616, A1
Geballe, T. R., Knapp, G. R., Leggett, S. K., et al. 2002, ApJ, 564, 466
Gharib-Nezhad, E., Iyer, A. R., Line, M. R., et al. 2021, ApJS, 254, 34
Gizis, J. E. 1997, AJ, 113, 806
Golimowski, D. A., Leggett, S. K., Marley, M. S., et al. 2004, AJ, 127, 3516
Gonzales, E. C., Burningham, B., Faherty, J. K., et al. 2020, ApJ, 905, 46
Gonzales, E. C., Burningham, B., Faherty, J. K., et al. 2021, ApJ, 923, 19
Gonzales, E. C., Faherty, J. K., Gagné, J., Artigau, É., & Bardalez Gagliuffi, D. 2018, ApJ, 864, 100
Gonzales, E. C., Faherty, J. K., Gagné, J., et al. 2019, ApJ, 886, 131
Hayashi, C., & Nakano, T. 1963, PThPh, 30, 460
Howe, A. R., McElwain, M. W., & Mandell, A. M. 2022, ApJ, 935, 107
Jones, H. R. A., Longmore, A. J., Allard, F., & Hauschildt, P. H. 1996, MNRAS, 280, 77
Karalidi, T., Marley, M., Fortney, J. J., et al. 2021, ApJ, 923, 269
Kass, R. E., & Raftery, A. E. 1995, J. Am. Stat. Assoc., 90, 773
Kataria, T., Sing, D. K., Lewis, N. K., et al. 2016, ApJ, 821, 9
Kellogg, K., Metchev, S., Gagné, J., & Faherty, J. 2016, ApJL, 821, L15
Kendall, T. R., Delfosse, X., Martín, E. L., & Forveille, T. 2004, A&A, 416, L17
Kirkpatrick, J. D. 2005, ARA&A, 43, 195
Kirkpatrick, J. D., Allard, F., Bida, T., et al. 1999, ApJ, 519, 834
Kirkpatrick, J. D., Barman, T. S., Burgasser, A. J., et al. 2006, ApJ, 639, 1120
Kirkpatrick, J. D., Cruz, K. L., Barman, T. S., et al. 2008, ApJ, 689, 1295
Kirkpatrick, J. D., Henry, T. J., & Liebert, J. 1993, ApJ, 406, 701
Kirkpatrick, J. D., Kellogg, K., Schneider, A. C., et al. 2016, ApJS, 224, 36
Kirkpatrick, J. D., Reid, I. N., Liebert, J., et al. 2000, AJ, 120, 447
Kitzmann, D., Heng, K., Oreshenko, M., et al. 2020, ApJ, 890, 174
Koen, C. 2013, MNRAS, 428, 2824
Kumar, S. S. 1963, ApJ, 137, 1121
Leggett, S. K., Geballe, T. R., Fan, X., et al. 2000, ApJL, 536, L35
Leggett, S. K., Golimowski, D. A., Fan, X., et al. 2002, ApJ, 564, 452
Lindegren, L., Hernandez, J., Bombrun, A., et al. 2018, A&A, 616, A2
Line, M. R., Knutson, H., Wolf, A. S., & Yung, Y. L. 2014, ApJ, 783, 70
Line, M. R., Marley, M. S., Liu, M. C., et al. 2017, ApJ, 848, 83
Line, M. R., Teske, J., Burningham, B., Fortney, J. J., & Marley, M. S. 2015, ApJ, 807, 183
Lodders, K. 1999, ApJ, 519, 793
Lodders, K. 2002, ApJ, 577, 974
Lodders, K. 2010, Exoplanet Chemistry (New York: Wiley), 157
Lodders, K., & Fegley, B. 2002, Icar, 155, 393
Lodders, K., & Fegley, B., Jr. 2006, Chemistry of Low Mass Substellar Objects (Chichester: Praxis Publishing Ltd.), 1

Lueber, A., Kitzmann, D., Bowler, B. P., Burgasser, A. J., & Heng, K. 2022, ApJ, 930, 136
Madhusudhan, N., & Seager, S. 2009, ApJ, 707, 24
Marley, M. S., Saumon, D., Visscher, C., et al. 2021, ApJ, 920, 85
Martin, E. C., Mace, G. N., McLean, I. S., et al. 2017, ApJ, 838, 73
McBride, B., & Gordon, S. 1994, Computer Program for Calculation of Complex Chemical Equilibrium Compositions and Applications I. Analysis Reference Publication NASA RP-1311 44135-319, https://www.grc.nasa.gov/WWW/CEAWeb/RP-1311.htm
McLean, I. S., Prato, L., McGovern, M. R., et al. 2007, ApJ, 658, 1217
Miles-Páez, P. A., Metchev, S. A., Heinze, A., & Apai, D. 2017, ApJ, 840, 83
Mohanty, S., & Basri, G. 2003, ApJ, 583, 451
Morley, C. V., Fortney, J. J., Kempton, E. M.-R., et al. 2013, ApJ, 775, 33
Morley, C. V., Fortney, J. J., Marley, M. S., et al. 2012, ApJ, 756, 172
Moses, J. I., Richardson, M. R., Madhusudhan, N., et al. 2012, AAS/Division for Planetary Sciences Meeting Abstracts, 44, 103.02
Moses, J. I., Line, M. R., Visscher, C., et al. 2013, ApJ, 777, 34
Patten, B. M., Stauffer, J. R., Burrows, A., et al. 2006, ApJ, 651, 502
Piette, A. A. A., & Madhusudhan, N. 2020, MNRAS, 497, 5136
Prato, L., Mace, G. N., Rice, E. L., et al. 2015, ApJ, 808, 12
Reid, I. N., Cruz, K. L., Kirkpatrick, J. D., et al. 2008, AJ, 136, 1290

Saumon, D., Hubbard, W. B., Burrows, A., et al. 1996, ApJ, 460, 993
Saumon, D., & Marley, M. S. 2008, ApJ, 689, 1327
Schmidt, S. J., West, A. A., Burgasser, A. J., Bochanski, J. J., & Hawley, S. L. 2010, AJ, 139, 1045
Schneider, A. C., Cushing, M. C., Kirkpatrick, J. D., et al. 2014, AJ, 147, 34
Sheppard, S. S., & Cushing, M. C. 2008, AJ, 137, 304
Skemer, A. J., Morley, C. V., Zimmerman, N. T., et al. 2016, ApJ, 817, 166
Sorahana, S., Yamamura, I., & Murakami, H. 2013, ApJ, 767, 77
Tinney, C. G., Reid, I. N., Gizis, J., & Mould, J. R. 1995, AJ, 110, 3014
van Altena, W. F., Lee, J. T., & Hoffleit, E. D. 1995, The General Catalogue of Trigonometric [Stellar] Parallaxes
Visscher, C. 2012, ApJ, 757, 5
Visscher, C., Lodders, K., & Fegley, B., Jr. 2006, ApJ, 648, 1181
Visscher, C., Lodders, K., & Fegley, B., Jr. 2010, ApJ, 716, 1060
Vrba, F. J., Henden, A. A., Luginbuhl, C. B., et al. 2004, AJ, 127, 2948
Wakeford, H. R., Visscher, C., Lewis, N. K., et al. 2017, MNRAS, 464, 4247
Yamamura, I., Tsuji, T., & Tanabé, T. 2010, ApJ, 722, 682
Zalesky, J. A., Line, M. R., Schneider, A. C., & Patience, J. 2019, ApJ, 877, 24
Zapatero Osorio, M. R., Caballero, J. A., & Béjar, V. J. S. 2005, ApJ, 621, 445
Zhang, Z. H., Pinfield, D. J., Gálvez-Ortiz, M. C., et al. 2017, MNRAS, 464, 3040